ROYAL SOCIETY OF CHEMISTRY

Check for updates

Transparent and flexible MXene-chitosan nanocomposite film for effective UV and high-energy blue light shielding applications†

Md. Hanif Munshi,[ab] Md. Didarul Islam,[c] M. Mehedi Hasan,[ad] Md Nasiruddin,[e] S. M. Fazle Rabbi, [iD][a] Shaikh Almoon Hussain [iD][a] and Md. Kamruzzaman [iD] *[a]

Facile, flexible and highly transparent nanocomposite films were synthesized *via* a solution casting approach by incorporating MXene nanoparticles into chitosan (CS) films and exhibited excellent UV and high-energy blue light absorbing ability. The prepared composite (CMX) films were characterized *via* ATR-FTIR, X-ray diffraction (XRD), FESEM, thermogravimetric analysis (TGA) and derivative thermogravimetric (DTG) analysis. ATR-FTIR spectroscopy, X-ray diffraction (XRD), and FESEM results confirmed that the MXene nanoparticles were uniformly distributed throughout the chitosan film, with strong hydrogen and static bonds formed between the two, while TGA and DTG data confirmed the thermal stability of the composite films. The moisture content (MC), water solubility (WS) index and water swelling (W) of the composite films were thoroughly monitored to investigate the efficiency of the films. CMX-0.04 composite films exhibited improved UV blocking performance: 99.55% of UV-A (320–400) nm, 100% of UV-B (280–320) nm, and 100% of UV-C (200–280) nm. Additionally, this film demonstrated exceptional absorption capabilities around 97.48% within the range of high-energy blue light (HEBL) (400–450 nm) radiation. Furthermore, addition of MXene nanoparticles in the CS film showed enhanced mechanical properties (tensile strength and Young's modulus of 80.09 ± 1.13 MPa and 19.72 ± 1.401 MPa, which was 303% and 830% higher than those of the pure CS film, respectively) with excellent film flexibility. This work offers a method to develop a composite film based on CS and MXenes, which has a lot of potential for expanding real-world applications in UV and HEBL blocking.

Sustainability spotlight

In this study, chitosan was initially produced from shrimp shells (in general, shrimp shells have almost no uses) as a renewable biomass source, which offer excellent environment-friendly reinforcement materials. Moreover, the fabricated MXene-incorporated chitosan composite (CMX) film exhibited excellent UV and HEBL shielding (absorbing) with almost no environmental impact. Besides, this research work addresses particularly the following UN sustainable development goals: "Make cities and human settlements inclusive, safe, resilient and sustainable (SDG 11)", "Ensure sustainable consumption and production patterns (SDG 12)" and "Take urgent action to combat climate change and its impacts (SDG 13)".

1 Introduction

Ultraviolet (UV) light is detrimental to human health, causing major injuries to the skin and even serious DNA damage, leading to skin cancer after prolonged exposure.[1–3] Solar radiation is the abundant supply of energy for photosynthesis and the vital heat source for the modern world's atmospheric circulation. This radiant energy emits 43% visible, 52% infrared and about 5% of UV light. Shorter wavelength UV light ranges from 315 to 400 nm (UV-A), 280 to 315 nm (UV-B), and 100 to 280 nm (UV-C). Almost 95% of UV-A and only 5% of UV-B reaches the earth surface, while UV-C is completely absorbed by the ozone layer.[4,5] Short-wavelength high-energy blue light (HEBL) in the 400–450 nm range travels through the cornea and lens to the retina, where it can lead to age-related macular degeneration, cataracts, and dry eyes. It can also stimulate the brain, suppress melatonin secretion, and increase the release of adrenocortical hormones, all of which can upset the hormonal balance and negatively impact the quality of sleep.[6,7] Some of

[a]Department of Applied Chemistry and Chemical Engineering, Faculty of Engineering, Gopalganj Science and Technology University, Gopalganj-8100, Bangladesh. E-mail: mkamruzzamandu81@gmail.com

[b]Department of Textile Engineering, Uttara University, Dhaka, 1230, Bangladesh

[c]National Institute of Textile Engineering and Research, University of Dhaka, Dhaka 1000, Bangladesh

[d]Department of Chemistry, Virginia Tech, Blacksburg, Virginia 24061, USA

[e]Department of Chemistry, Faculty of Science, Gopalganj Science and Technology University, Gopalganj-8100, Bangladesh

the modern electronic tools such as mobile phones, monitor screens, tablets, and flat televisions that use various lamps (LEDs and CFLs) also emit HEBL and UV radiation.[5] Therefore, it is crucial to develop new light-shielding materials with excellent transparency in visible-light regions and that can efficiently block UV light and blue light.

Chitosan (CS) is a bioactive polymer that contains an unbranched chain (β-(1,4)-2-amino-2-deoxy-D-glucopyranose) in its backbone. It is insoluble in water (pK_a is approximately 6.5) and shows suitable solubility in acidic media because of its positively charged primary amine groups.[8] CS is synthesized from chitin after extensive deacetylation. Chitin is mostly derived from the leftover shells of crustaceans (shrimp, prawn, crab, and lobster). Crustacean shells primarily consist of chitin (15–40%), protein (20–40%), calcium and magnesium carbonate (20–50%), and other minor ingredients.[9,10] Moreover, chitosan is the second most naturally available cationic polysaccharide which exhibited excellent biocompatibility, great biodegradability, low immunogenicity, brilliant film-forming ability and good antibacterial properties.[11–14] Therefore, CS has found diverse applications in agriculture, biomedicine, bioengineering, cosmetics, food packaging, textile, wastewater treatment, and so on.[13,15,16] Although the neat CS film is considered as an ideal material for the fabrication of polymeric films, it possesses several drawbacks including the lack of ability to scavenge UV, HEBL rays and free radicals. Therefore, the incorporation of macromolecules or nanoparticles into CS films is one of the feasible approaches.

Most recently, several inorganic nanoparticles such as TiO_2, ZnO, CeO_2, MnO_2, graphene, and MXenes have been used, which exhibit shielding ability.[17,18] Those materials are blended with polymeric reinforced structures which provide the synergistic effect of both reinforced polymeric materials and nanoparticles. In this study, MXenes were used as nanoparticles on CS-reinforced materials. MXenes show some unique properties including non-toxicity, hydrophilicity, high chemical and thermal stability, adsorption ability, perfect crystal structure, tuneable energy gap, surface activities, large exposed surface area, and optoelectronic and electrochemical properties.[19–21] For this reason, MXenes have

been extensively applied in saturable absorbers, biomedicine, energy storage, sensors, electromagnetic interference shielding, catalysis, conductive electrodes, and biological and environmental protection gears.[22–26] It has been reported that $Ti_3C_2T_x$ (as MXene) possesses a narrow band gap (0.9–1.75 eV) and exhibits high-efficiency UV absorption.[27] In a study, it was found that the MXene (Ti_3C_2) can significantly increase UV absorption from 15% to 90% at 400 nm when added to water-borne polyurethane (WPU).[27] The band gap of MXenes can be adjusted for the absorption of suitable electromagnetic radiation.[27] Besides, having a 2D structure influences the reflection of radiation, which can be facilitated for the adsorption of harmful UV radiation.[28] Hence, MXenes and MXene composites have become a hot topic for UV shielding application around the world.[29]

In this study, a flexible and transparent composite CMX film was fabricated at room temperature by a simple film casting method, which exhibited excellent UV and HEBL shielding. The applications of the fabricated CMX films as coating/shielding materials are illustrated in Fig. 1. The transparent composite films were then subjected to a variety of structural and morphological studies, including FTIR (Fourier transform infrared) spectroscopy, FESEM (field emission scanning electron microscopy), and XRD. The film's performance under UV and HEBL irradiation was evaluated by UV-Vis spectroscopy, while thermogravimetric analysis (TGA) and derivative thermogravimetric (DTG) analysis were performed to investigate the thermal stability of the composite films. Moisture content (MC), water solubility index (WS) and water swelling (W) of composite films were thoroughly monitored to investigate the efficiency of the film. Furthermore, the mechanical properties (breaking load, tensile strength, and Young's modulus) and flexibility of the CMX film were studied and compared with the control CS film.

2 Materials and methods

2.1. Materials

MXene ($Ti_3C_2T_x$) of research grade was purchased from Sigma-Aldrich. Sodium hydroxide Pellet (NaOH, 98%) was purchased from Loba Chemie Pvt. Ltd (India). Hydrochloric acid (HCl,
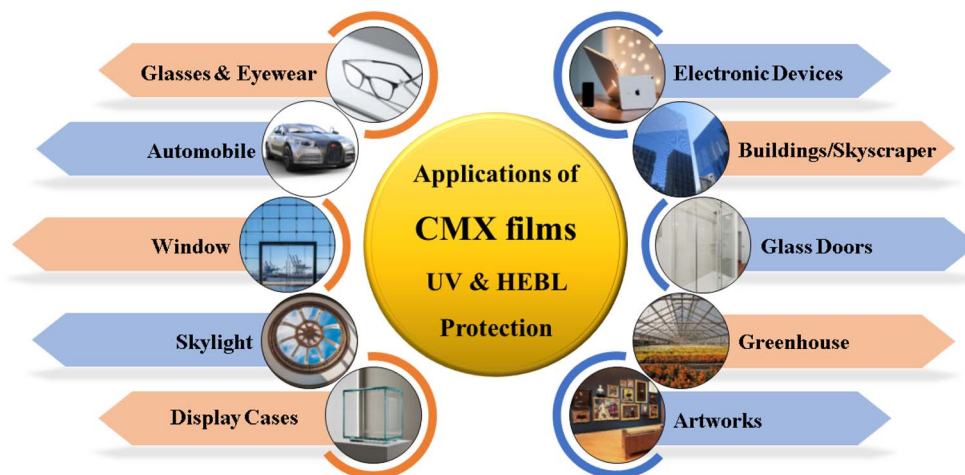

Fig. 1 Schematic representation of CMX film applications.

37%) and acetic acid (CH_3COOH, glacial) were purchased from Merck (Germany). For the fabrication of the CMX film, deionized water (DI) was used.

2.2. Synthesis of chitosan

Over the past few decades, researchers have developed several methods to extract CS from shrimp shells.[30,31] In this study, CS was extracted following a modified method described by Rashid *et al.*[30] The schematic of CS synthesis from shrimp shell *via* a chemical extraction process is illustrated in Fig. S1.† According to this method, shrimp shells were washed several times with DI water, dried and then crushed. First, the crushed shells were treated with 0.5 M HCl solution in a solution ratio of 1/5 w/v at room temperature to facilitate the removal of inorganic minerals for 6 hours. Then, wet shrimp shells were demineralized with 1 M HCl solution at room temperature for 12 hours, maintaining an approximate solution ratio of 1/8. After neutralization with DI water, wet shrimp shells that had been demineralized were dried at 65 °C overnight. The demineralized shrimp sample was then deproteinized at room temperature for 24-hours using 0.75 M NaOH (1 : 5 w/v) under agitation at 300 rpm. After completing deproteinization (which is known as chitin), the alkali-insoluble fraction was washed with DI water until attaining a neutral pH. The dried chitin was de-acetylated by reflux heating in an oil bath at 120 °C with 12 M NaOH solution (1 : 10 w/v) for 12 h producing CS. After complete deacetylation, the sample was washed until attaining a neutral pH. Finally, the obtained CS fraction was dried under continuous air flow.

2.3. Fabrication of CMX films

The schematic of the CMX film fabrication is presented in Fig. 2. To prepare a 5 wt% CS solution, 0.5 g of CS powder was dissolved into 100 ml glacial acetic acid (0.1%) solution with continuous stirring at 300 rpm for about 24-hours. After that, the CS solution was centrifuged at 2000 rpm for 30 min to remove insoluble CS particles and was vacuum filtered to obtain a more stable, clear and uniformly distributed solution. Different amounts (0.05, 0.1, 0.2 and 0.4 mg mL^{-1}) of MXene powder were evenly dispersed in DI water *via* probe sonication for 2-hours. Then, 0.005, 0.01, 0.02 and 0.04 wt% MXene solution was added dropwise into the clear uniform 5 wt% CS solution (1 : 1 v/v) under vigorous stirring (350 rpm) at room temperature for 6 hours. After that, 25 ml of a uniform CMX solution was casted in a 90 mm polystyrene Petri dish. The CMX solution was dried at 32 ± 2 °C for 48 hours to achieve a uniform and clean CMX film. A set of CMX films were fabricated and labeled as pure CS, CMX-0.005, CMX-0.01, CMX-0.02, and CMX-0.04, respectively. Fig. 3a illustrates the orientations of MXenes to the CS nanofibers based on these interactions.

3 Material characterization

3.1. X-ray diffraction (XRD) analysis

The X-ray diffraction (XRD) patterns of pristine CS and CMX films were acquired using an Ultima IV Rigaku Corporation Japan, which was applied to estimate the distance between crystal planes, known as the interplanar spacing, and to obtain information about the crystal symmetry, orientation, and crystalline phase. The diffractometer was operated with CuK radiation in continuous mode at a scan rate of 4° min^{-1} in the 5–80° range with a step width of 0.04°.

3.2. Fourier transform infrared analysis

FTIR spectra of pure CS, MXene and CMX films were recorded using a Nicolet 6700 spectrometer (Thermo Fisher Scientific,
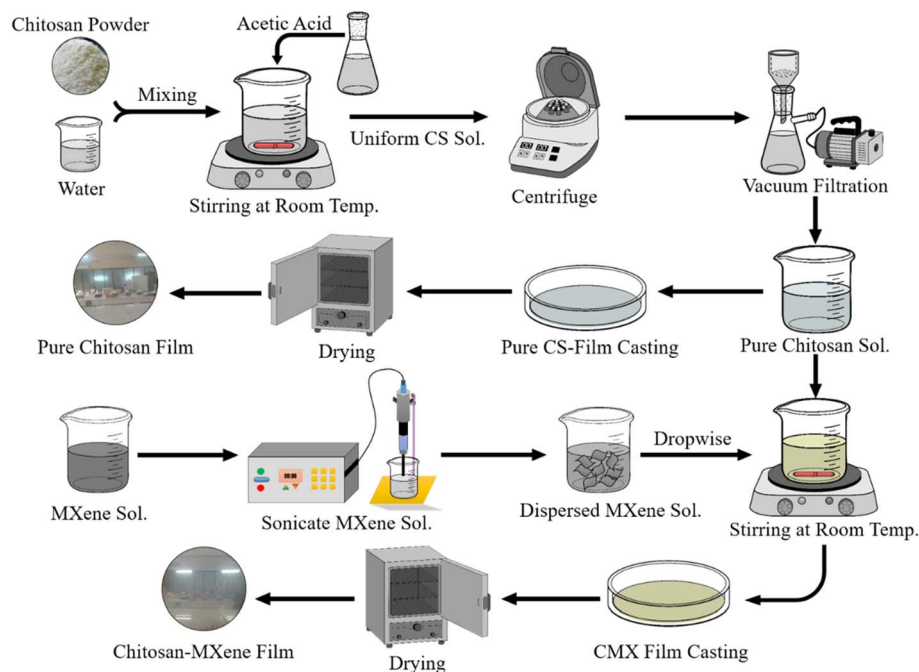

Fig. 2 Fabrication process of the UV-protective CMX film.
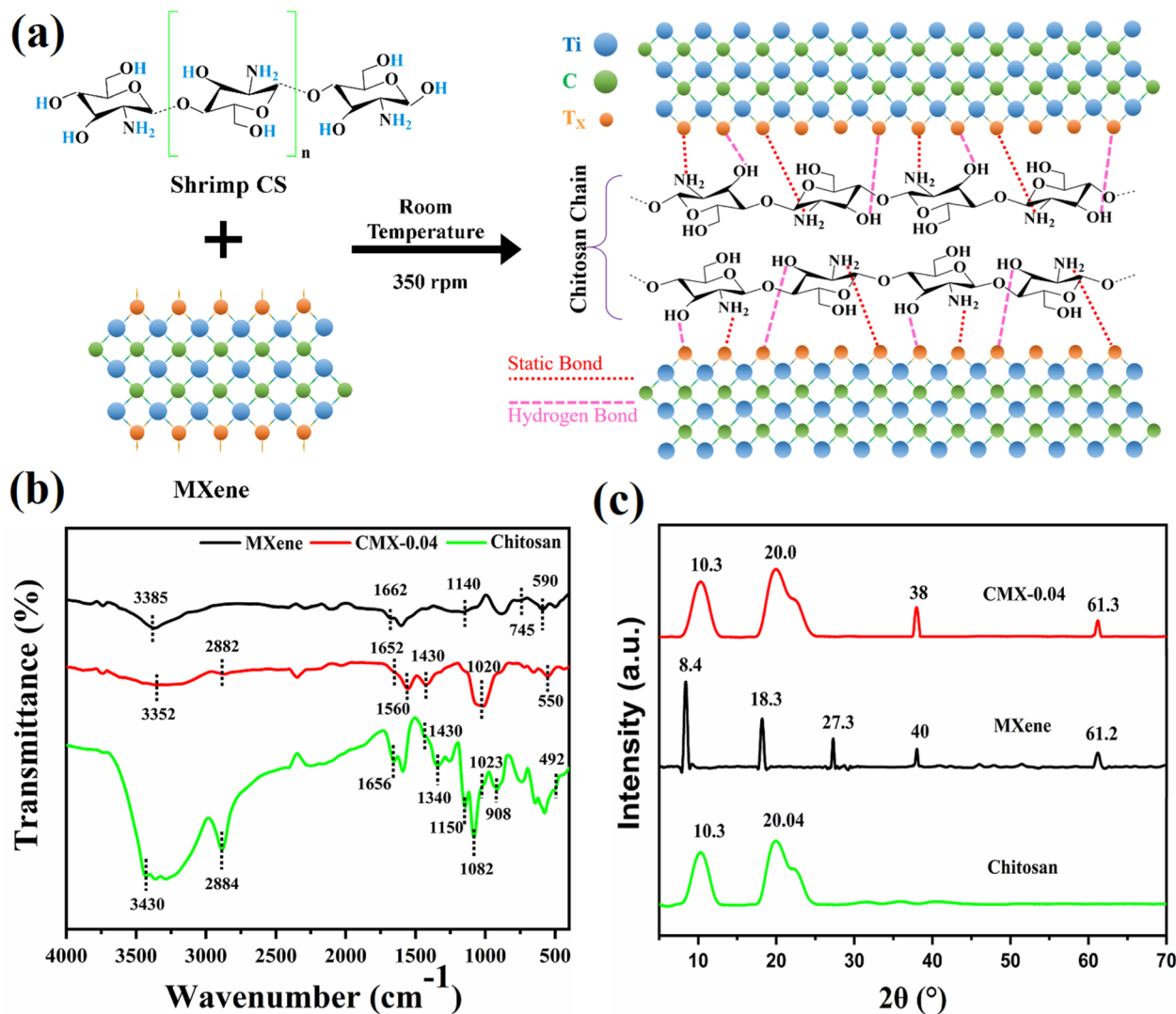
Paper

Fig. 3 (a) Probable interactions and reactions among MXenes and the synthesized CS polymer chain. (b) ATR-FTIR spectra of pure CS, MXene powder and the CMX-0.04 film. (c) XRD spectrum of pure CS, MXene powder and the CMX-0.04 film.

USA). The attenuated total reflectance (ATR) mode was used to scan the spectra in the 500–4000 cm^{-1} range.

3.3. Morphological analysis

The surface morphologies of MXenes and CMX composite films were observed using a ZEISS Sigma 350 VP with a Schottky-type field emission filament (FEG-Field Emission Gun) equipped with a Gemini column. Following dehydration, the gold–palladium-coated MXenes and CMX films were prepared for SEM investigation with a resolution of up to 10 nm. Energy-dispersive X-ray (EDX) spectroscopy and elemental mapping were performed using a Bruker X-ray EDX detector. The images were acquired using a secondary detector (SE2) in the high-vacuum mode to determine the presence of different chemical components in the CMX films.

3.4. Film thickness and opacity measurement

The film thickness was measured using a digital electronic micrometer (SYATEK, India) with a resolution of 0.001 mm

(0.00005″). The thickness was measured before any other tests were conducted. The thickness was measured at five sites for each film and the average values were considered.[32]

Using a UV-Vis spectrophotometer (Shimadzu, Japan), the light barrier properties of the film were measured. The films were cut into 1×4 cm^2 sections and then attached to the quartz cell cuvette. Their absorbance was measured at 600 nm using an empty cuvette as the ref. 33. Further, the film opacity was calculated using eqn (1):

$$\text{Opacity}\left(\text{mm}^{-1}\right) = \frac{\text{Absorbance at 600 nm}}{\text{Thickness of film(mm)}} \quad (1)$$

3.5. Moisture content (MC) measurement

The moisture content (MC) of the film was examined using the method described by Costa et al.[34] According to this method, the coated films were cut into pieces of dimensions 2×2 cm^2, weighed and subsequently dried at 105 °C for 24 h. The MC was

then measured as the percentage of moisture removed from the films according to eqn (2):

$$MC\ (\%) = \frac{M_i - M_f}{M_i} \times 100 \qquad (2)$$

where M_i and M_f are the weights of the initial and dried samples, respectively. Measurements were taken three times, and the average was then calculated.

3.6. Water solubility (%WS) and swelling property (%W)

The gravimetric approach was used to determine the films' WS. According to this technique, the coated films were sliced into $2 \times 2\ cm^2$ pieces, weighed, and then dried at 105 °C for 24 hours. The initial dry weight (W_i) was then calculated and weighed to the closest 0.0001 g. The dried samples were stored in a glass beaker with 100 mL of distilled water and gently shaken at 25 °C for 24 hours. The final dry weight (W_f) was measured by drying the remaining undissolved film at 105 °C for 24 hours until its weight remained constant.[32] Triplicate tests were conducted for each type of film. Eqn (3) was used to obtain the solubility in water (%):

$$\%WS\ (\%) = \frac{W_i - W_f}{W_i} \times 100 \qquad (3)$$

The gravimetric approach was used to measure the swelling (water retention). Each film was sliced into three $2 \times 2\ cm^2$ samples, which were subsequently preserved for five days in desiccators. The sample was then weighed, which was termed W_{dry}. After that, the samples were kept at 25 °C for 24 hours in an airtight container with 100 mL of distilled water. The wet sample was pressed between two filter papers to eliminate surface water, which was then weighed and termed W_{wet}.[35] Eqn (4) was used to assess each sample's water retention (%W):

$$\%W\ (\%) = \frac{W_{wet} - W_{dry}}{W_{dry}} \times 100 \qquad (4)$$

3.7. UV and HEBL shielding performance of the film and evaluation

A PG Instruments T82 UV/VIS spectrophotometer was used to measure the UV-visible transmittance of pure CS and CMX films between 200 and 900 nm in wavelength, with air serving as a reference. The blocking performance of the films was evaluated using the following eqn (5)–(8). Transmittance spectra ($T\%$) were used to estimate the UV and HEBL protection afforded by the films.[5]

UV-C blocking(200 − 280 nm) percentage(%)

$$= 100 - \frac{\int_{200}^{280} T d\lambda}{\int_{200}^{280} d\lambda}\ (\%) \qquad (5)$$

UV-B blocking(280 − 315 nm)percentage(%)

$$= 100 - \frac{\int_{280}^{315} T d\lambda}{\int_{280}^{315} d\lambda}\ (\%) \qquad (6)$$

UV-A blocking(315 − 400 nm)percentage(%)

$$= 100 - \frac{\int_{315}^{400} T d\lambda}{\int_{315}^{400} d\lambda}\ (\%) \qquad (7)$$

HEBL blocking(400 − 450 nm)percentage(%)

$$= 100 - \frac{\int_{400}^{450} T d\lambda}{\int_{400}^{450} d\lambda}\ (\%) \qquad (8)$$

where $d\lambda$ is the bandwidth, λ is the wavelength, and $T(\lambda)$ is the average spectral transmittance of the film.

3.8. Thermogravimetric analysis (TGA)

TGA of the prepared CMX films and synthesized CS was performed using a TGA-50 thermal analyzer (SHIMADZU, Japan). A steady nitrogen gas flow rate of 2 mL min^{-1} and a constant heating rate of 10 °C min^{-1} were maintained, while 1.5 mg of samples were heated from 30 to 800 °C in order to perform the analysis.

3.9. Mechanical properties analysis

The mechanical properties including tensile strength (TS), Young's modulus, and percentage elongation (E) at break of pure CS and CMX films (rectangular strips of 5 cm by 1.5 cm) were examined using a modified version of ASTM standard 638.[36] A James Heal Ultimate Tensile Tester was used to evaluate all the mechanical properties. The films were held between two jaws with a 3 cm gauge length throughout the experiment. Following that, a 40% break detection was programmed, while the upper arm was raised at a rate of 20 mm per minute. The following formulas are used to determine each film's mechanical characteristics (TS, E, and YM).

$$TS = \frac{F}{A} \qquad (9)$$

$$YM = \frac{UTS}{S} \qquad (10)$$

$$E = \frac{L - L_o}{L_o} \times 100 \qquad (11)$$

where A is the original cross-sectional area of films, TS is the tensile strength, F is the maximum stress that a material can sustain without breaking, YM is Young's modulus, UTS is the ultimate tensile strength of films, L is the length of the film following force application prior to fracture, S is the strain, E is the elongation at break, L_o is the initial length of films, and L is the total length preceding fracture. The average of five duplicate samples was taken for each value.

4 Results and discussion

4.1. ATR-FTIR analysis

ATR-FTIR analysis was performed to examine the surface functional groups of neat CS, MXene, and MXene-incorporated films (CMX-0.04) against transmittance mode, as illustrated in Fig. 3b and Table S2.† The ATR-FTIR spectrum of neat CS

showed peaks at 3430 cm^{-1} that indicated the stretching vibration of –OH and –NH$_2$ group of amines. The absorption bend at around 2884 cm^{-1} was due to the C–H asymmetric stretching. The lower intensity of absorption peaks at 1656 cm^{-1} (C=O stretching of amide I) and 1340 cm^{-1} (C–N stretching of amide II) indicated almost complete deacetylation of chitin. The absorption band at 1150 cm^{-1} (corresponding to the asymmetric stretching of the C–O–C bridge/O$_2$ of glycosidic linkage), 1082 and 1032 cm^{-1} (skeletal vibrations involving the C–O stretching) were characteristic of its saccharide structure.[10] A pyranose ring was found in shrimp CS at around 908 cm^{-1}. The intensity of the amide group peak at 3430 cm^{-1} and the carbonyl group at 1656 cm^{-1} varied as the deacetylation process progressed. The spectra between 1430 and 492 cm^{-1} revealed the existence of CH$_3$, CH$_2$, and CH groups in addition to the primary and secondary –OH groups, that were attached to the pyranose ring.[37]

In the spectrum of MXenes, a prominent band at 3385 cm^{-1} was observed, attributed to the stretching vibration of –OH. The peaks at 1140, 745 and 590 cm^{-1} may be associated with Ti–F, Ti–O and Ti–C, respectively.[38] Stretching bands at approximately 3552 cm^{-1} and 1662 cm^{-1} were assigned to the carbonyl groups (–OH and C=O) in the prepared CMX composite.[39,40] Most of the above peaks of MXene were found in CMX composite film FTIR spectrum. However, the changes in intensity and the shifting of certain bands indicating the bond formation between the MXene and chitosan with in CMX film.

Furthermore, the CMX composite displays the same –F (550 cm^{-1}), –O (1652 cm^{-1}), and –OH groups as MXenes.[41] At 3352 cm^{-1}, an N–H stretching vibration band was observed. Additionally, the amide group (–NH–CO–) peak in the CMX composite was located at 1652 and 1560 cm^{-1}.[42] Moreover, the absorption bends at 2884 and 1430 cm^{-1} confirm the presence –CH$_2$ groups in both CS and CMX films.[43] The notable shift towards a lower wavenumber (red shift) was observed in the primary characteristic peaks from 3430, 1590 and 1023 cm^{-1} to 3352, 1560 and 1020 cm^{-1}, indicating the presence of inter- or intramolecular interaction between CS and MXenes in the composite CMX film.[44] Moreover, in the CMX composite film, there was a drastic decrease in absorption peaks at 3352 and 1652 cm^{-1}, which was also an indication of hydrogen bond formation between MXenes and CS.[45] The orientations and interactions of MXenes and CS within the CMX composite are depicted in Fig. 3a.

4.2. XRD analysis

XRD spectrum was used to investigate the arrangement and crystalline nature of the pure MXene, CS film and CMX film. As illustrated in Fig. 3c, the synthesized shrimp CS exhibited a characteristic diffraction peak at 20.04° (020), which indicates the semi-crystalline nature. Moreover, these peaks are an indication of the organized arrangement of the CS chain within the polymer matrix with a d-spacing of 0.43 nm.[46] Meanwhile, an MXene powder exhibited several sharp peaks (as shown in Fig. S2†) at 8.4° (002), 18.3° (004), 27.3° (006), 40° (104) and 61.2° (110), which are in good agreement with the literature.[47,48]

Moreover, the sharpness of all the mentioned peaks for MXenes confirmed higher crystallinity with a very ordered well-organized lattice structure. Furthermore, the synthesized CMX composite film showed four major characteristic peaks at 10.30°, 20.0°, 38° and 61.3°, indicating excellent attachment between CS and MXenes. The peak shifting (slide) toward a lower angle showed an increase in the d-spacing. Conversely, the peak intensity of the MXene decreased sharply, which was an indication of the loss of crystallinity within the CMX film.[49]

4.3. Morphological characterization

The high-resolution FE-SEM image displayed in Fig. 4 provides insights into the morphology and structure of the MXene and CMX-0.04 layer. FEM-SEM analysis showed that the MXene had a typical accordion-like multilayer morphology (Fig. 4a).[50] It can be observed that the MXene particles were dispersed uniformly across the CMX film. From the SEM images, it was clearly observed that the MXene and CS were strongly interpenetrated within the CMX composite film, as shown in Fig. 4c with a thickness of around 2.84 μm. Moreover, from Fig. 4b, it was found that MXene nanosheets were uniformly distributed throughout the CMX composite film, producing a smooth surface. The entanglement between the MXene and CS, which results in their intimate integration and imparts a greater mechanical characteristics than the pristine CS film, was also confirmed from Fig. 4b and c. This observation was made in a previous study.[51] The probable interconnection network between the MXene and the CS polymer chain is schematically illustrated in Fig. 3a.

The EDX provides insights into the synthetic products' elemental analysis. Fig. 4i displays the EDX spectra of the CMX-0.04 film. The presence of C (33.57%), O (28.76%), Ti (23.83%), F (10.94%), and N (2.90%) was confirmed by EDX analysis. The spectra show O and F due to their presence as MXene surface terminations (Tx = –OH, –O, –F, *etc.*). The high C and O contents are due to CMX inbuilt high ratio in CS. In addition, Fig. 4d–h show the colored square elemental mapping (type of EDX analysis) of the CMX-0.04 film. Moreover, the corresponding mappings of C, O, and N elements (Fig. 4e, f and h) indicate that the shrimp CS was evenly distributed through the film.[52] The elemental maps also confirmed the composition and distribution of MXenes (Ti, C, F and O) in the composite film.[50] The development of oxides such as TiO$_2$ and a surface termination group comprising F, OH, and O are the reasons why O in the MXene element was seen in EDX.[53] The EDX mapping demonstrated the uniform dispersion inside the CMX-0.04 film in addition to its exceptional purity.[44]

4.4. TGA analysis

Thermal properties of the synthesized CS, MXene and CMX-0.04 films were analyzed by thermogravimetric and derivative thermogravimetric analyses (Fig. 5). A slight decrease in weight (2.083%) was noted between 50 and 800 °C, suggesting the thermal stability of the 2D MXene. The thermal properties of CMX-0.04 films were clearly impacted by the addition of MXenes. Nevertheless, the deterioration patterns of the CMX-
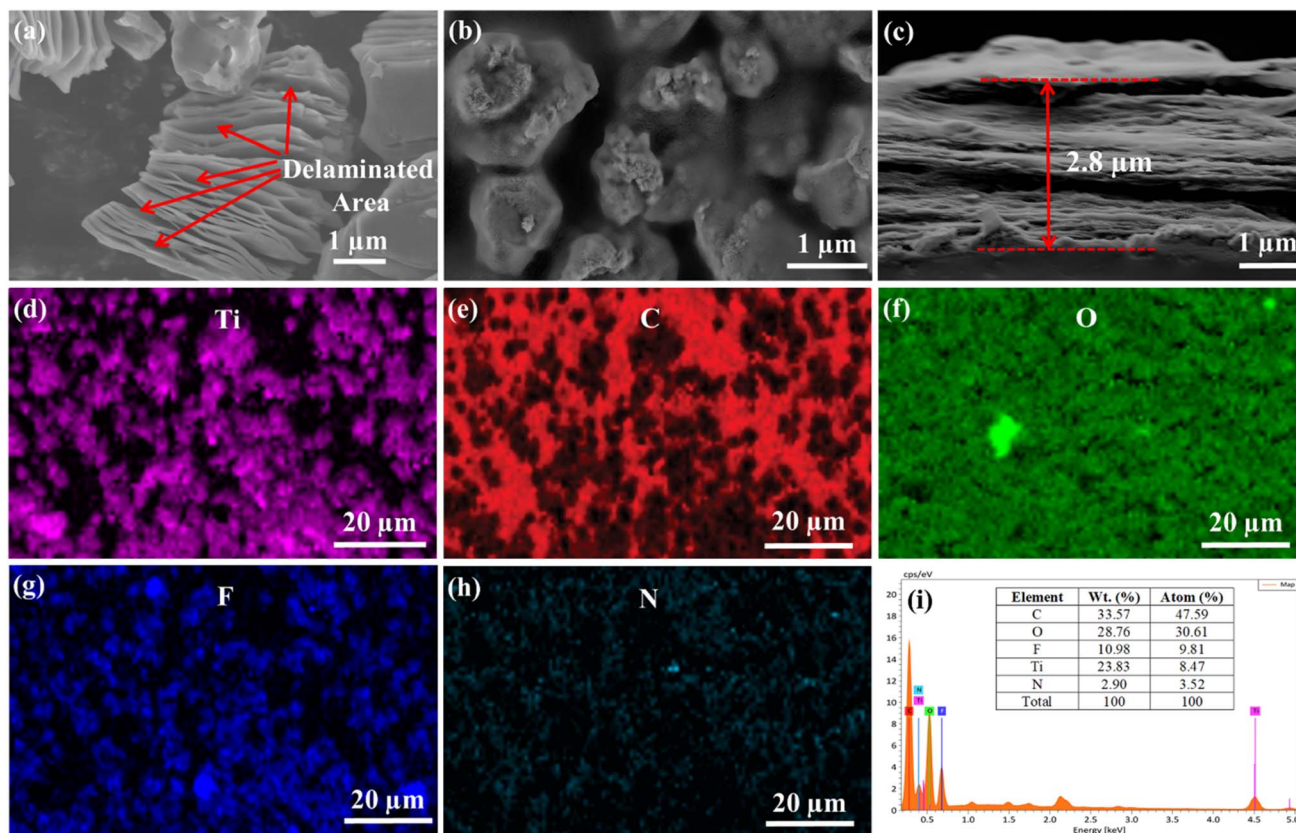
Fig. 4 FE-SEM images of (a) MXenes, (b) CMX-0.04 (film surface) and (c) CMX-0.04 (cross-sectional). Corresponding EDX-Mapping of Ti (d), C (e), O (f), F (g) and N (h). (i) EDX spectrum of the CMX-0.04 film.

0.04 and neat CS films were almost similar. Table S6† summarizes the temperature at which 5% (T_{onset}), 50% (T_{50}), and maximum (T_{MAX}) weight loss occurred in addition to weight losses at different stages and char percentages. Due to the incorporation of MXenes in CS, T_{onset} of the CMX-0.04 film increased from 65.4 °C to 87 °C; similarly, T_{50} also increased from 444 °C for pure CS to 495 °C for CMX-0.04. This indicates that the thermal stability of the films was slightly increased due

to the presence of MXenes. Furthermore, the ultimate weights that remained fixed after 800 °C for the neat CS and CMX-0.04 were 7.4% and 17.6%, respectively. These results further suggest that the addition of MXenes to CS improved the films' thermal stability.

The films' degradation patterns (CS and CMX-0.04) may be separated into three stages: room temperature (RT) to 210 °C, 210 °C to 410 °C, and above 410 °C. In the first stage, weight loss
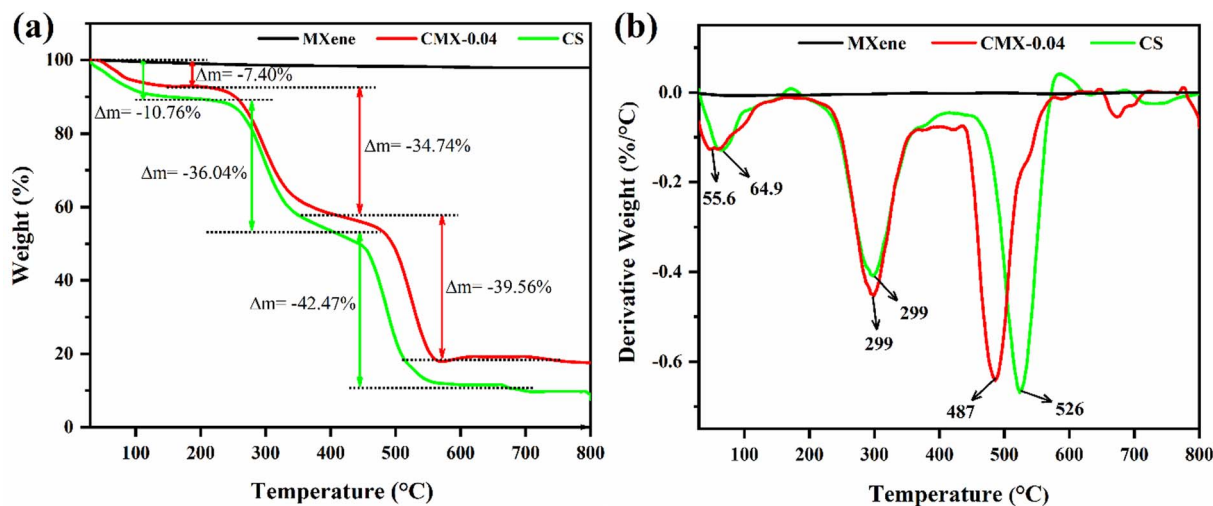

Fig. 5 (a) TGA and (b) DTG thermogram of MXenes, pure CS and the CMX-0.04 film.

dropped from 10.76% for neat CS to 7.4% for CMX-0.04 from RT to 210 °C. The weight loss in this zone is primarily attributed to the water loss from CS due to hydrogen bonding facilitated by abundant hydroxyl and amino groups present within CS.[54] The films began to degrade quickly above 210 °C and continued to do so until 410 °C. Weight losses at this stage were almost similar for both CS and CMX-0.04 film (about 36.04% and 34.74%); however, as Fig. 5b illustrates, the DTG curve clearly shows that the rate of deterioration of pure CS was significantly higher than that of the CMX-0.04 film. The second stage of degradation, which was associated with oxidative degradation involving carbon created by chain reactions within CS, manifests in the temperature range of 200 to 410 °C. At the third stage (above 410 °C), degradation emerges between 410 and 560 °C with the weight loss of 39.56% (CMX-0.04) and pure 42.47% (CS). At about 450 °C, CS and CMX-0.04 films show maximum degradation.[55] Moreover, after the complete TGA experiment, 7.4% and 17.6% char residue (Table S6†) were formed for CS and CMX-0.04 films, indicating the improvement of the film thermal behavior with the incorporation of MXene nanosheets. Furthermore, the weight loss rate (Fig. 5a) of CMX-0.04 was found to be lower than that of the neat CS film. The aforementioned discussion may indicate that adding MXenes can increase the film's thermal stability.

4.5. Thickness and optical properties

All the prepared films demonstrated flexibility, handling ability, and transparency. Table 1 displays the total thickness and opacity of each film. The thickness is one of the major parameters that affects the film's behavior and characteristics, including its mechanical, optical, and water-interaction qualities.[32] The thickness of the CS and composite CMX films ranged from 0.009 to 0.016 mm (Table S1†). The table indicates that the film thickness is a function of MXene concentration, meaning that it increases as the MXene content increases (except for CMX-0.002).

The pure CS film had a very translucent surface, but CMX films were darker and less transparent than the pure CS film. High opacity, low transparency, and color of the CMX film might block UV-visible light from passing through films.[56] The greater the visible light transmittance, the more transparent the films and the lower their opacity; higher opacity implies good light barrier function.[57] Consequently, because of the light blocking ability of multilayer MXenes, their incorporation into CMX could make the films opaquer and improve their barrier function against UV rays.[58] The MXene assembly improved the

Table 1 Thickness and opacity of the CS and CMX films[a]

Samples	Thickness (mm)	%T600	Abs600	Opacity (mm^{-1})
Pure CS	0.0104 ± 0.001	91.2	0.040	3.85
CMX-0.005	0.0122 ± 0.001	68.1	0.168	13.77
CMX-0.01	0.0138 ± 0.0008	44.7	0.356	25.80
CMX-0.02	0.0126 ± 0.002	30.0	0.524	41.59
CMX-0.04	0.0144 ± 0.002	14.0	0.864	60.00

[a] Abs600 is the absorbance at 600 nm.

interaction between the CS molecules and the MXene surface functional group, making the film structure more compact and increasing the opacity of the CMX films. Hence, the opacity of the CMX films was much higher than that of the pure CS films. In comparison to the pure CS film, the opacity of the CMX-0.02 and CMX-0.04 films was 41.59% and 60%, respectively.

4.6. UV-Vis transmittance characterization

MXenes are dispersed in shrimp-synthesized CS at different concentrations to form CMX films. To create CMX films, MXenes are distributed at varying quantities in the CS film. The digitized images of the CMX films are shown in Fig. 6c and d. From Fig. 6c and d it was evident that the composite films were fairly transparent with transmittances close to the neat CS film and almost no obvious localized aggregation of MXene particles was found within the composite film. However, the transparency appears to decrease as the amount of Mxene is increased. Moreover, the composite film exhibited excellent flexibility, which is demonstrated using digital photographs, as shown in Fig. 6d.

Fig. 6a and b and Table S3† summarize the transmittance and blocking towards ultraviolet, HEBL to visible wavelengths, which were measured using the UV-Vis spectra of pure CS and CMX (CMX-0.005, CMX-0.01, CMX-0.02, and CMX-0.04) films. Over 90% transmittance was shown by the CS film in the visible spectrum, nearly 83% and 72% in the UV-A and UV-B ranges, respectively, and 53% in the UV-C range. Transmittance was observed to be greatly reduced when MXenes were added to the composite films.
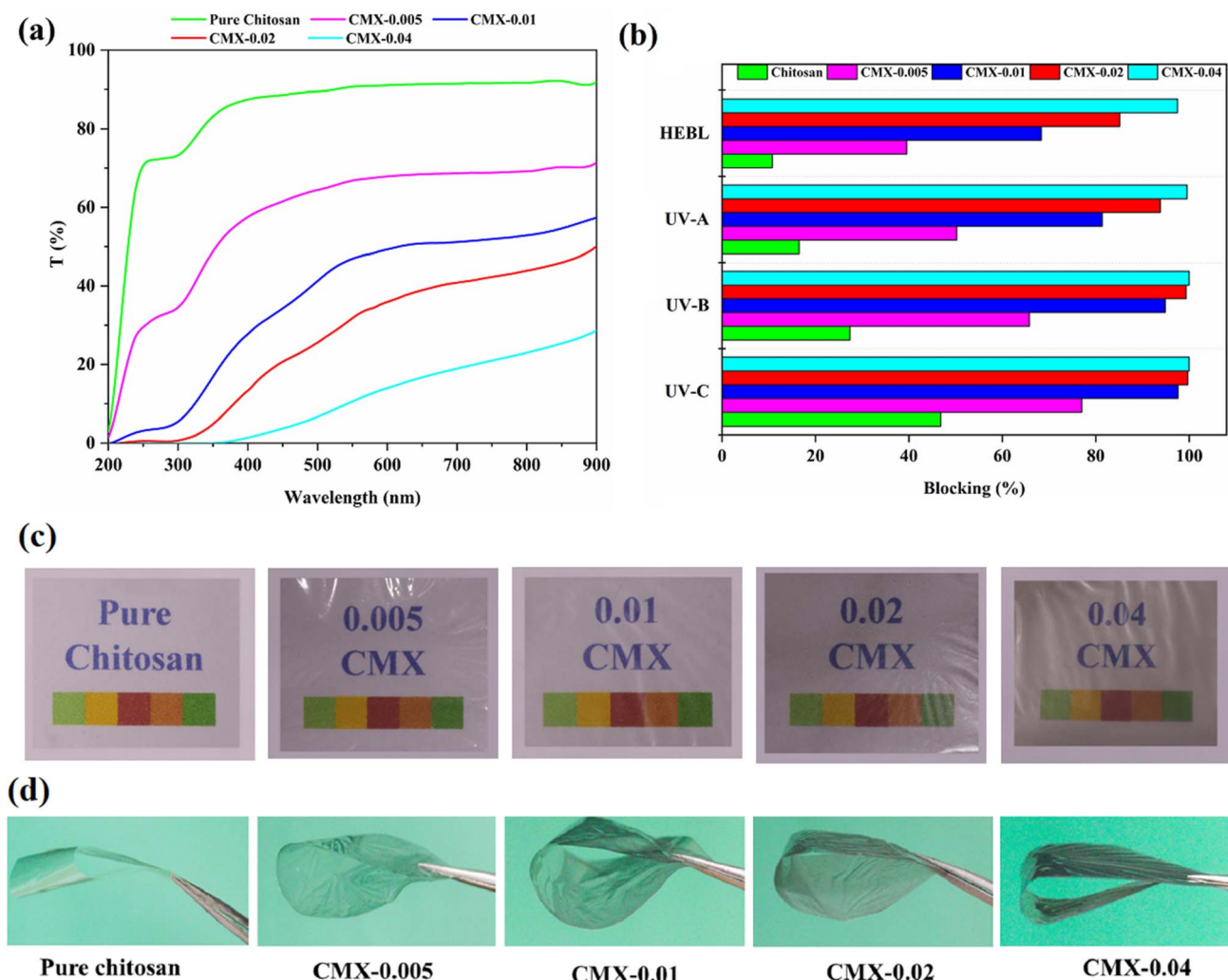
In the visible region, transmittance has been reduced by over 23% by adding 0.005% MXenes. Compared to CMX-0.005, the UV regions had a nearly 22% significant decrease in absorbance, while the visible area's transmittance was dramatically reduced for CMX-0.01. However, as Fig. 6a and b illustrate, UV absorbance was observed to rise by nearly 14% when the MXene content is increased from 0.01 to 0.02 and 0.04. Although the films were less transparent in the visible spectrum than CMX-0.005, the CMX-0.01 film blocked around 81% of UV-A, 95% of UV-B, and 97.6% of UV-C rays. Following the pattern, the film's capacity to block UV light was also enhanced by increasing the MXene content to 0.02%. However, CMX-0.02 demonstrated a 12% increase in UV-A blocking and a roughly 6% increase in UV-B and UV-C blocking when compared to CMX-0.01. In contrast to all CMX films, the CMX-0.04 film remarkably blocks ∼100% of the UV region. The UV blocking and transparency mechanism of the composite films can be assigned to the collaborative effect of absorption and reflection ability of the MXene nanosheets.[59] In a recent study, considerable large absorption and lower reflection have suggested an strong absorption-dominant UV shielding behaviour of MXene nanosheets.[60,61] The UV absorption of MXene nanosheets can be due to the presence of transition metal elements posing partially filled d-orbitals, which can absorb UV photons.[62] Moreover, the presence of surface terminal groups including –OH and –F can contribute to the UV absorption. Furthermore, uniform dispersion of multi-layered MXene nanosheets within

Fig. 6 (a) Effect of the MXene-loaded CS film in different regions of solar radiation (UV and HEBL region). (b) UV rays and HEBL rays blocking the performance of CS and the CMX films. (c) Digital photographs of the transparent films of pure CS and MXene-incorporated composite film. (d) Digital photographs of pure CS and MXene-incorporated composite film demonstrating flexibility.

the polymer composite reflect or scatter the UV irradiation, resulting in a reduction of penetration of solar irradiation.[63,64] However, the ultrathin thickness with high alignment of MXenes ensures the high transparency of the composite films.[65] Therefore, the CMX composite film exhibited high-energy UV shielding with excellent transparent within the visible light irradiation. Along with UV blocking, it was found that when the MXene level increased from pure CS to CMX-0.04 (Fig. 6b), HEBL shielding also improved from about 9 to about 85.5%.

Film blocking and transmittance behavior can be attributed to the combined action of MXene's UV absorbance capacity and its 2D planar geometry.[66] Conversely, a decrease in transmittance in the visible range was observed in the case of CMX films. The decrease in the visible spectrum may result from the multilayered MXene within the CMX film that absorbs the solar radiation or may be due to the solar radiation absorbing ability of the MXene. Moreover, the presence of functionalized groups within the MXene surface (such as –OH, –O, or –F) resulted in an interaction with the solar light. The increasing amount of –OH

groups on MXene nanosheets was confirmed by the SEM with EDX analysis.[67] The negatively charged MXene surface terminations T_x (–F, –O, and –OH) and the positively charged nitrogen-containing groups (NH_3^+) or surface groups (–OH and –NH_2) of CS are anticipated to interact in two different ways at the organic–inorganic interface.[43,44] Furthermore, the surface terminal groups of the MXene and CS film may form hydrogen bonds with one another. In general, electrostatic interactions come first, followed by non-covalent interactions.[68,69]

The UV shielding performance of MXene-loaded CMX films (CMX-0.02 and CMX-0.04) is compared with the shielding materials reported in the literature, which is tabulated in Fig. 7 and 8.[12,70–76] In comparison to the other films, it was found that the CMX-0.04 film performs better at UV shielding in all UV areas.

4.7. Moisture content (MC), water swelling (W) and water solubility (WS)

Enhancing the water resistance of the synthetic materials is vital for their use in practical applications in the local
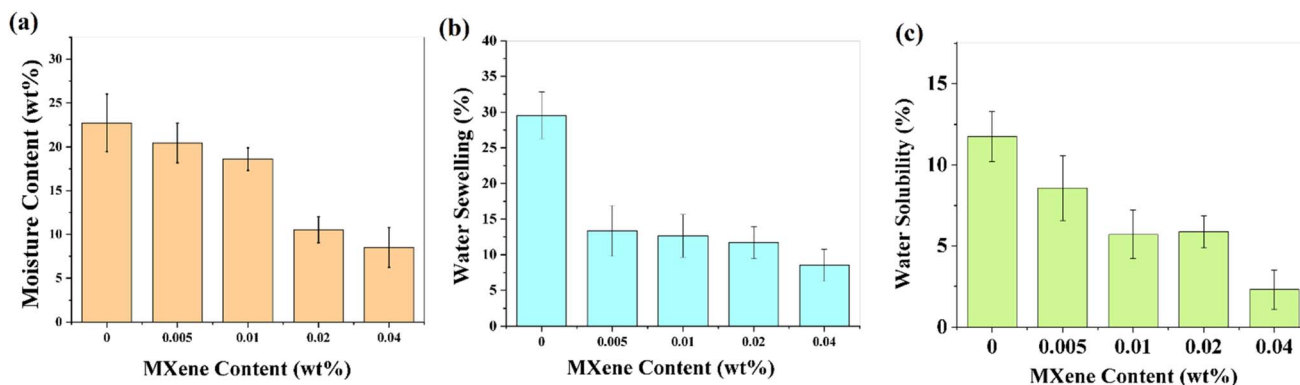
Fig. 7 (a) Moisture content (MC), (b) swelling index (%W), and (c) water solubility (%WS) of the prepared films.
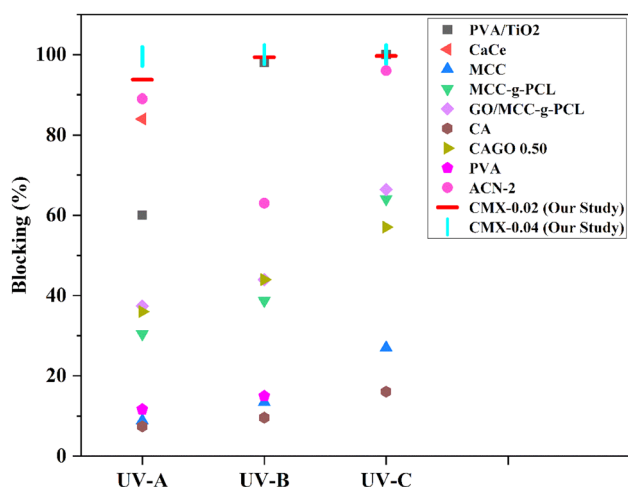

Fig. 8 UV radiation blocking performance of CMX nanocomposite films compared with other UV shielding materials available in the literature.[12,70–76]

environment. Fig. 7a displays the MC of pure CS and CMX films. The pure CS film exhibited the highest MC (%), because of the high hydrophilicity (presence of hydroxyl and amine groups) of pure CS, which readily absorbs moisture, making it highly susceptible to water interaction.[77] The addition of 0.005 to 0.04 wt% MXene reduced the moisture absorption from 22.73% to 8.51%, respectively (Table S5†). This may be due to the reduction in the number of hydrophobic sites in the polymeric chain or may be due to the agglomeration of the MXene nanoparticles between the polymeric chains, so that the free space of the CS polymer has been reduced to impregnate the water molecules inside the polymer and create a dense compact network.[69,78]

As the MXene was incorporated into the CS film, the films' swelling progressively decreased from 29.55 to 8.51%, as shown in Fig. 7b and Table S5.† The network density and hydration capacity of polymers generally have an impact on the swelling.[79] First, the CS films absorbed water and began to swell, and an amino group of CS was simultaneously protonated.[80] Owing to their structure, pure CS films had a significant swelling capacity that was more than that of the other films and roughly twice

that of the CMX films. Because of the characteristics of MXenes (hydrophilicity, high specific surface area, abundant surface functional groups) and interactions (hydrogen and electrostatic bond) between the CMX composites, it exhibits excellent water retention properties.[81] Notably, the swelling changes gradually decreased (8.57, 5.71, 5.88 and 2.312) with the increase in MXene content, resulting from the reactions between the adjacent MXene and CS. Because MXenes are hydrophilic, water molecules were absorbed into the interlayer region, causing a little swelling effect in MXene-based (CMX) films.[82] Water diffusion, ionization of amino or carboxyl groups, dissociation of hydrogen and ionic bonds, and polymer relaxation all contributed to the film's swelling.[83]

The water solubility of the film is an important factor for shielding materials used in real-world applications. In general, the hydrophilicity of the material influences the films' solubility, which in turn decrees its intended usage or applications.[84] Fig. 7c shows that the film's water solubility varied from 11.76 to 2.32% (Table S5†). Despite being insoluble in water, the results indicated that CS had a low solubility value of 11.8%. Due to its unique property, CS-based materials may be used as edible and degradable films.[85] The primary factor restricting its water solubility was the presence of intra- and intermolecular hydrogen bonds within the polymer chain. CS is only water-soluble at pH < 6 because its amino groups can get partially protonated in acidic environments, which causes repulsion between positively charged macro chains and allows water molecules to diffuse and subsequently solvate macromolecules.[86] The result also showed that after increasing the MXene content from 0.005 wt% to 0.04 wt% in CS, the water solubility of CMX films decreased.

4.8. Mechanical properties

Fig. 9 illustrates the mechanical parameters (TS, % E, and YM) of neat CS and composite CMX films. The breaking load and elongation (%) of CS film were 3.04 N and 9.2%, which is an indication of film flexibility, while a lower value of breaking load indicates the lower load bearing ability. However, by the incorporation of MXenes from 0.005 to 0.04% of the CS weight, the breaking load were gradually increased to 15.3 N, although
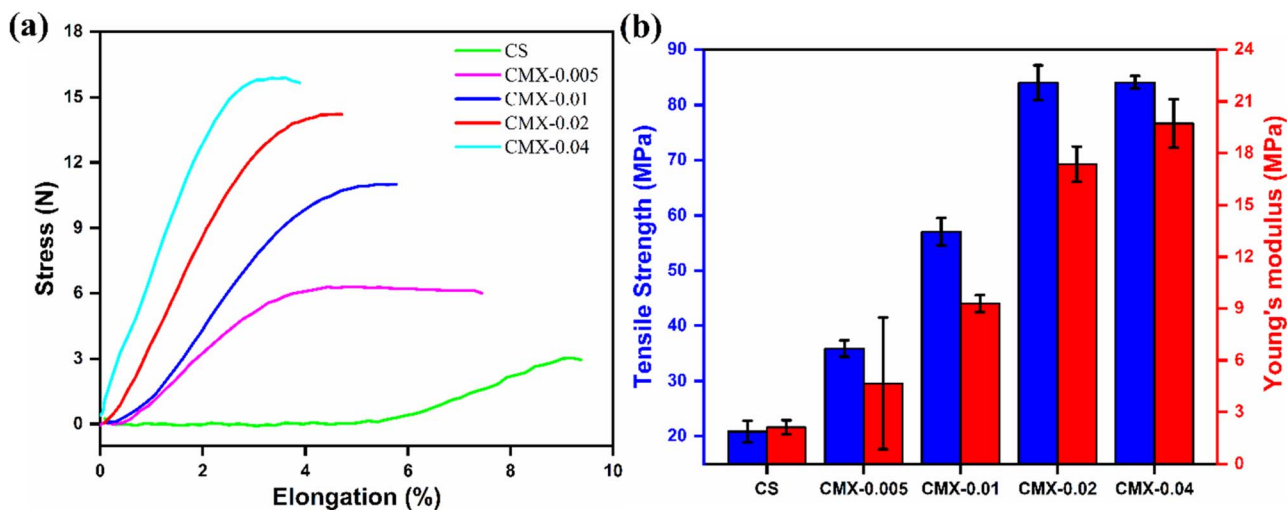
Fig. 9 Mechanical properties: (a) stress *vs.* percentile elongation and (b) tensile strength and Young's modulus of the prepared films.

the % elongation values were gradually decreased (Fig. 9a). Two factors contributed to the composite film's increased breaking load: (a) improved mechanical interlocking and increased chemical bonding, particularly hydrogen bonding between the MXene and the polymer matrix; and (b) the filling of MXene molecules in the empty space between polymer chains, which formed a more compact structure and improved the film's crystalline nature.[87,88] Moreover, an improved mechanical property (more than 303 and 830% enhanced tensile strength and Young's modulus) was found for the CMX-0.04 composite film compared to the neat CS film (20.83 MPa and 2.12 MPa of tensile strength and Young's modulus respectively) (Fig. 9b). Almost similar results of breaking load, elongation, tensile strength and Young's modulus were found for the CMX-0.02 and CMX-0.04 composite film. This may be due to the saturation of MXenes within the CS film. Further addition of the MXene into the CS may result in a significant reduction in the mechanical property due to the agglomeration of MXene nanoparticles. However, the incorporation of MXenes into the CS film results in a significant reduction in breaking elongation. One possible explanation for the reduction in breaking elongation is the composite film's stiffness or rigidity and the restriction of polymer chain mobility, due to the increase in chemical bonding (hydrogen bonding) between CS and the MXene.

Conclusion

In this study, a transparent flexible composite film was successfully fabricated by the incorporation of MXene nanoparticles (0.005 to 0.04%) into a CS host polymeric film which can be used as a UV and HEBL shielding material. ATR-FTIR analysis confirmed the formation of hydrogen bonds among polymers and MXenes and no residual acetic acid content in coatings. FESEM confirmed the uniform distribution of MXenes throughout the film. Moreover, the incorporation of MXenes results in an improved thermal stability. An improved

mechanical property (more than 303 and 830% enhanced tensile strength and Young's modulus) was found for the CMX-0.04 composite film compared to the neat CS film. The CMX-0.04 composite films, most significantly, demonstrated enhanced UV and HEBL blocking capabilities, achieving 99.55% of UV-A (320–400) nm, 100% of UV-B (280–320) nm, 100% of UV-C (200–280) nm, and 97.48% of HEBL (400–450) nm. Based on the outcomes of the investigations, the CMX composite films possess a lot of potential in UV and HEBL shielding applications.

Data availability

The data supporting this article have been included as part of the ESI.†

Author contributions

Md. Kamruzzaman established the process concept. Md. Hanif Munshi and Md. Didarul Islam performed the experimental work. Md. Hanif Munshi and Md. Didarul Islam performed data analysis and data interpretation. Md. Kamruzzaman and M. Mehedi Hasan supervised the work. The manuscript was written through contributions of all the authors. All the authors have given approval to the final version of the manuscript.

Conflicts of interest

The authors declare no competing financial interest.

Acknowledgements

References

1 Y. Jiang, K. Dong, J. An, F. Liang, J. Yi, X. Peng, C. Ning, C. Ye and Z. L. Wang, *ACS Appl. Mater. Interfaces*, 2021, **13**, 11205–11214.

2 C. Chen, Z. Xu, J. Qiu, W. Ye, X. Xu, R. Wang, C. Hu, J. Zhuang, B. Lei and W. Li, *ACS Appl. Nano Mater.*, 2022, **5**, 9140–9149.

3 X. Tang, T. Yang, D. Yu, H. Xiong and S. Zhang, *Environ. Int.*, 2024, 108535.

4 J. Tian and J. Yu, *J. Photochem. Photobiol., B*, 2009, **97**, 152–160.

5 B. K. Barman, A. Hashimoto and T. Nagao, *ACS Sustain. Chem. Eng.*, 2021, **9**, 9879–9890.

6 K. Su, Y. Tao and J. Zhang, *J. Mater. Sci.*, 2021, **56**, 17353–17367.

7 Z.-C. Zhao, Y. Zhou, G. Tan and J. Li, *Int. J. Ophthalmol.*, 2018, **11**, 1999.

8 M. M. Islam, S. Biswas, M. S. Islam, M. Shahruzzaman, M. M. Hasan, M. D. Islam, P. Haque and M. M. Rahman, in *Marine Biomaterials*, 2022, pp. 281–315.

9 N. I. W. Azelee, D. Dahiya, S. Ayothiraman, N. M. Noor, Z. I. Abd Rasid, A. N. M. Ramli, B. Ravindran, F. U. Iwuchukwu and R. Selvasembian, *Int. J. Biol. Macromol.*, 2023, **253**, 126492.

10 R. S. C. M. de Queiroz Antonino, B. R. P. Lia Fook, V. A. de Oliveira Lima, R. Í. de Farias Rached, E. P. N. Lima, R. J. da Silva Lima, C. A. Peniche Covas and M. V. Lia Fook, *Mar. Drugs*, 2017, **15**, 141.

11 C. Vilela, R. J. B. Pinto, J. Coelho, M. R. M. Domingues, S. Daina, P. Sadocco, S. A. O. Santos and C. S. R. Freire, *Food Hydrocolloids*, 2017, **73**, 120–128.

12 R. Zhong, Q. Zhong, M. Huo, B. Yang and H. Li, *Int. J. Biol. Macromol.*, 2020, **146**, 939–945.

13 A. Tozar and İ. H. Karahan, *Surf. Coat. Technol.*, 2018, **340**, 167–176.

14 K. Wang, J. Zhuang, Y. Liu, M. Xu, J. Zhuang, Z. Chen, Y. Wei and Y. Zhang, *Carbohydr. Polym.*, 2018, **184**, 445–452.

15 A. S. Rasal, Y. H. Chen, K. Dehvari, G. Getachew, P. J. Tseng, K. Waki, S. Bela and J. Y. Chang, *Mater. Today Energy*, 2021, **19**, 100615.

16 G. Amor, M. Sabbah, L. Caputo, M. Idbella, V. De Feo, R. Porta, T. Fechtali and G. Mauriello, *Foods*, 2021, **10**, 121.

17 H. K. Singh, S. Kumar, J. Bamne, K. Taiwade, N. Singh, V. Chandel and F. Z. Haque, *Mater. Today: Proc.*, 2021, **46**, 5607–5618.

18 M. P. Puttaswamy, N. Kundachira Subramani, S. Shivanna, N. Gumatapura Siddamallappa, M. Beejaganahalli Sangameshwara and R. G. Urs, *J. Appl. Polym. Sci.*, 2024, **141**, e55837.

19 Y. Song, Y. Chen, X. Jiang, Y. Ge, Y. Wang, K. You, K. Wang, J. Zheng, J. Ji and Y. Zhang, *Adv. Opt. Mater.*, 2019, **7**, 1801777.

20 K. Maleski, C. E. Ren, M.-Q. Zhao, B. Anasori and Y. Gogotsi, *ACS Appl. Mater. Interfaces*, 2018, **10**, 24491–24498.

21 Q. Wu, S. Chen, Y. Wang, L. Wu, X. Jiang, F. Zhang, X. Jin, Q. Jiang, Z. Zheng and J. Li, *Adv. Mater. Technol.*, 2019, **4**, 1800532.

22 S. K. Avinashi, R. K. Mishra, R. Singh, R. Shweta, Z. Fatima and C. R. Gautam, *ACS Appl. Mater. Interfaces*, 2024, **16**, 47003–47049.

23 L. Jin, X. Guo, D. Gao, C. Wu, B. Hu, G. Tan, N. Du, X. Cai, Z. Yang and X. Zhang, *NPG Asia Mater.*, 2021, **13**, 24.

24 H. Riazi, G. Taghizadeh and M. Soroush, *ACS Omega*, 2021, **6**, 11103–11112.

25 R. Bhardwaj and A. Hazra, *J. Mater. Chem. C*, 2021, **9**, 15735–15754.

26 M. He, Y. Huang, X. Zhang, W. Zhu, W. Shao, J. Wang, D. Xu and W. Yao, *Int. J. Biol. Macromol.*, 2024, **264**, 130821.

27 T.-Y. Zhang, H. Wang, J. Tong, J. Zhang, X. Wang and Y. Zeng, *Compos. Commun.*, 2022, **33**, 101235.

28 A. Ahmed, B. Adak, T. Bansala and S. Mukhopadhyay, *ACS Appl. Mater. Interfaces*, 2020, **12**, 1687–1697.

29 K. Raagulan, R. Braveenth, B. M. Kim, K. J. Lim, S. B. Lee, M. Kim and K. Y. Chai, *RSC Adv.*, 2020, **10**, 1613–1633.

30 T. U. Rashid, M. M. Rahman, S. Kabir, S. M. Shamsuddin and M. A. Khan, *Polym. Int.*, 2012, **61**, 1302–1308.

31 M. Yadav, P. Goswami, K. Paritosh, M. Kumar, N. Pareek and V. Vivekanand, *Bioresour. Bioprocess.*, 2019, **6**, 1–20.

32 P. Cazón, M. Vázquez and G. Velazquez, *Biomacromolecules*, 2019, **20**, 3115–3125.

33 M. Ahmed, A. K. Verma and R. Patel, *J. Food Process. Preserv.*, 2022, **46**, e16485.

34 M. J. Costa, M. A. Cerqueira, H. A. Ruiz, C. Fougnies, A. Richel, A. A. Vicente, J. A. Teixeira and M. Aguedo, *Ind. Crops Prod.*, 2015, **66**, 305–311.

35 P. Cazón, M. Vázquez and G. Velazquez, *Biomacromolecules*, 2019, **20**, 2084–2095.

36 Shimadzu, *Tensile Properties of Rigid and Semi-rigid Plastics* (ASTM D638 and ISO 527), 2017.

37 T. K. Varun, S. Senani, N. Jayapal, J. Chikkerur, S. Roy, V. B. Tekulapally, M. Gautam and N. Kumar, *Vet. World*, 2017, **10**, 170.

38 T. Parker, D. Zhang, D. Bugallo, K. Shevchuk, M. Downes, G. Valurouthu, A. Inman, B. Chacon, T. Zhang and C. E. Shuck, *Chem. Mater.*, 2024, **36**, 8437–8446.

39 M. Li, P. Zhang, Q. Wang, N. Yu, X. Zhang and S. Su, *Polymers*, 2023, **15**, 2110.

40 S. Shuai, Z. Huang, V. E. Burov, V. Z. Poilov, F. Li, H. Wang, R. Liu, S. Zhang, C. Cheng and W. Li, *Int. J. Min. Sci. Technol.*, 2023, **33**, 379–387.

41 N. R. Azeez, S. S. Salih, M. Kadhom, H. N. Mohammed and T. K. Ghosh, *Green Chem. Eng.*, 2024, **5**, 339–347.

42 H. Wan, L. Nan, H. Geng, W. Zhang and H. Shi, *Processes*, 2021, **9**, 524.

43 E. A. Mayerberger, R. M. Street, R. M. McDaniel, M. W. Barsoum and C. L. Schauer, *RSC Adv.*, 2018, **8**, 35386–35394.

44 F. Zhang, Z. Qi, X. Han, H. Cai and K. Yang, *Sustainable Energy Fuels*, 2024, **8**, 3680–3687.

45 S. Mushtaq, S. M. Husnain, S. A. R. Kazmi, Y. Abbas, J. Jeon, J. Y. Kim and F. Shahzad, *Sci. Rep.*, 2023, **13**, 19696.

46 S. Lokesh Kumar, A. Servesh, V. R. Sunitha, J. R. Prasad, S. Tabassum, S. G. Ramaraj, N. Kumar and S. Govindaraju, *Polym. Adv. Technol.*, 2024, **35**, 1–12.

47 M. A. Iqbal, A. Tariq, A. Zaheer, S. Gul, S. I. Ali, M. Z. Iqbal, D. Akinwande and S. Rizwan, *ACS Omega*, 2019, **4**, 20530–20539.

48 H. Fang, Y. Pan, M. Yin and C. Pan, *J. Mater. Sci. Mater. Electron.*, 2019, **30**, 14954–14966.

49 A. Tariq, S. I. Ali, D. Akinwande and S. Rizwan, *ACS Omega*, 2018, **3**, 13828–13836.

50 J. Isailović, A. Oberlintner, U. Novak, M. Finšgar, F. M. Oliveira, J. Paštika, Z. Sofer, N. Tasić, R. Gusmão and S. B. Hočevar, *ACS Appl. Mater. Interfaces*, 2023, **15**, 31643–31651.

51 Y. Wan, P. Xiong, J. Liu, F. Feng, X. Xun, F. M. Gama, Q. Zhang, F. Yao, Z. Yang, H. Luo and Y. Xu, *ACS Nano*, 2021, **15**, 8439–8449.

52 Z. Liu, N. Li, P. Liu, Z. Qin and T. Jiao, *ACS Omega*, 2022, **7**, 5570–5577.

53 B. Saini, H. K, D. Laishram, R. Krishnapriya, R. Singhal and R. K. Sharma, *ACS Appl. Nano Mater.*, 2022, **5**, 9319–9333.

54 Y. Liu, T. Zhang, B. Yang, M. Hao, X. Hu and X. Wang, *ACS Appl. Polym. Mater.*, 2024, **6**, 12983–12991.

55 H. Niu, Z. Xiao, P. Zhang, W. Guo, Y. Hu and X. Wang, *Sci. Total Environ.*, 2024, **908**, 168261.

56 G. da Silva Filipini, V. P. Romani and V. Guimarães Martins, *Packag. Technol. Sci.*, 2021, **34**, 91–103.

57 K. Li, J. Zhu, G. Guan and H. Wu, *Int. J. Biol. Macromol.*, 2019, **122**, 485–492.

58 X. Liu, W. Zhang, X. Zhang, Z. Zhou, C. Wang, Y. Pan, B. Hu, C. Liu, C. Pan and C. Shen, *Nat. Commun.*, 2024, **15**, 3076.

59 T. Yun, H. Kim, A. Iqbal, Y. S. Cho, G. S. Lee, M. K. Kim, S. J. Kim, D. Kim, Y. Gogotsi, S. O. Kim and C. M. Koo, *Adv. Mater.*, 2020, **32**, 1–9.

60 F. Shahzad, M. Alhabeb, C. B. Hatter, B. Anasori, S. Man Hong, C. M. Koo and Y. Gogotsi, *Science*, 2016, **353**, 1137–1140.

61 J. Liu, H. Zhang, R. Sun, Y. Liu, Z. Liu, A. Zhou and Z. Yu, *Adv. Mater.*, 2017, **29**, 1702367.

62 V. Soni, P. Singh, H. H. P. Quang, A. A. P. Khan, A. Bajpai, Q. Van Le, V. K. Thakur, S. Thakur, V.-H. Nguyen and P. Raizada, *Chemosphere*, 2022, **293**, 133541.

63 B.-M. Jun, S. Kim, H. Rho, C. M. Park and Y. Yoon, *Chemosphere*, 2020, **254**, 126827.

64 J. Kim, K. H. Lee, S. Lee, S. Park, H. Chen, S. K. Kim, S. Yim, W. Song, S. S. Lee, D. H. Yoon, S. Jeon and K.-S. An, *Chem. Eng. J.*, 2023, **453**, 139973.

65 X. Zhang, Z. Zhang and Z. Zhou, *J. Energy Chem.*, 2018, **27**, 73–85.

66 M. Q. Mehmood, A. R. Shah, M. A. Naveed, N. Mahmood, M. Zubair and Y. Massoud, *IEEE Access.*, 2023, **11**, 130287–130295.

67 Y. Zhou, Y. Lin, B. Tawiah, J. Sun, R. K. K. Yuen and B. Fei, *ACS Appl. Mater. Interfaces*, 2021, **13**, 21876–21887.

68 M. Boota, M. Pasini, F. Galeotti, W. Porzio, M.-Q. Zhao, J. Halim and Y. Gogotsi, *Chem. Mater.*, 2017, **29**, 2731–2738.

69 O. Mashtalir, M. R. Lukatskaya, M.-Q. Zhao, M. W. Barsoum and Y. Gogotsi, in *MXenes*, Jenny Stanford Publishing, 2023, pp. 401–414.

70 M. M. Hasan, M. S. Hossain, M. D. Islam, M. M. Rahman, A. S. Ratna and S. Mukhopadhyay, *ACS Appl. Mater. Interfaces*, 2023, **15**, 32011–32023.

71 H. Ju, Y. Jiang, B. Xue, Y. Xu, H. Guo, M. Huo and F. Li, *New J. Chem.*, 2018, **42**, 9260–9268.

72 H. Sadeghifar, R. Venditti, J. Jur, R. E. Gorga and J. J. Pawlak, *ACS Sustain. Chem. Eng.*, 2017, **5**, 625–631.

73 Y. Yu, X. Gao, Z. Jiang, W. Zhang, J. Ma, X. Liu and L. Zhang, *RSC Adv.*, 2018, **8**, 10865–10872.

74 A. C. M. De Moraes, P. F. Andrade, A. F. De Faria, M. B. Simões, F. C. C. S. Salomão, E. B. Barros, M. D. C. Gonçalves and O. L. Alves, *Carbohydr. Polym.*, 2015, **123**, 217–227.

75 M. E. Culica, A. L. Chibac-Scutaru, V. Melinte and S. Coseri, *Materials*, 2020, **13**, 1–15.

76 Y. Wang, J. Su, T. Li, H. Bai, Y. Xie, M. Chen and W. Dong, *ACS Appl. Mater. Interfaces*, 2017, **9**, 36281–36289.

77 J. Xia, H. Zhang, F. Yu, Y. Pei and X. Luo, *ACS Appl. Mater. Interfaces*, 2020, **12**, 24370–24379.

78 M. Dong, G. Mastroianni, E. Bilotti, H. Zhang and D. G. Papageorgiou, *ACS Sustain. Chem. Eng.*, 2024, **12**, 11056–11066.

79 R.-D. Pavaloiu, A. Stoica-Guzun, M. Stroescu, S. I. Jinga and T. Dobre, *Int. J. Biol. Macromol.*, 2014, **68**, 117–124.

80 J. Nunthanid, S. Puttipipatkhachorn, K. Yamamoto and G. E. Peck, in *Drug Development and Industrial Pharmacy*, Taylor & Francis, 2001, vol. 27, pp. 143–157.

81 L. Zhao, H. Xu, L. Liu, Y. Zheng, W. Han and L. Wang, *Adv. Sci.*, 2023, **10**, 2303922.

82 Y. Li, J. Zhu, H. Cheng, G. Li, H. Cho, M. Jiang, Q. Gao and X. Zhang, *Adv. Mater. Technol.*, 2021, **6**, 2100410.

83 S. Mathew, M. Brahmakumar and T. E. Abraham, *Biopolymers*, 2006, **82**, 176–187.

84 S. Hajji, A. Chaker, M. Jridi, H. Maalej, K. Jellouli, S. Boufi and M. Nasri, *Environ. Sci. Pollut. Res.*, 2016, **23**, 15310–15320.

85 K. M. Kim, J. H. Son, S. Kim, C. L. Weller and M. A. Hanna, *J. Food Sci.*, 2006, **71**, E119–E124.

86 I. A. Sogias, V. V Khutoryanskiy and A. C. Williams, *Macromol. Chem. Phys.*, 2010, **211**, 426–433.

87 Y. Ni, H. Nie, J. Wang, J. Lin, Q. Wang, J. Sun, W. Zhang and J. Wang, *Food Chem.*, 2022, **366**, 130539.

88 A. Ahmed, B. Adak, T. Bansala and S. Mukhopadhyay, *ACS Appl. Mater. Interfaces*, 2019, **12**, 1687–1697.